Simulations of Solid–Liquid Scalar Transfer for a Spherical Particle in Laminar and Turbulent Flow

J. J. Derksen
School of Engineering, University of Aberdeen, Aberdeen, Scotland AB24 3UE, U.K

DOI 10.1002/aic.14384
Published online in Wiley Online Library (wileyonlinelibrary.com)

Scalar transfer from a solid sphere to a surrounding liquid has been studied numerically. The simulation procedure involves full hydrodynamic resolution of the solid–liquid interaction and the flow (laminar and turbulent) of the carrier fluid by means of the lattice-Boltzmann method. Scalar transport is solved with a finite volume method on coupled overlapping domains (COD): an outer domain discretized with a cubic grid and a shell around the solid sphere with a spherical grid with fine spacing in the radial direction. The shell is needed given the thin scalar boundary layer around the sphere that is the result of high Schmidt numbers (up to Sc = 1000). After assessing the COD approach for laminar benchmark cases, it is applied to a sphere moving through homogeneous isotropic turbulence with the sphere radius larger (by typically a factor of 10) than the Kolmogorov length scale so that it experiences an inhomogeneous hydrodynamic environment. This translates in pronounced scalar concentration variations and transfer rates over the sphere's surface. Overall scalar-transfer coefficients are compared to those derived from classical Sherwood number correlations. © 2014 American Institute of Chemical Engineers *AIChE J*, 60: 1202–1215, 2014
Keywords: solid–liquid flow, scalar transport, turbulence, lattice-Boltzmann method, finite volume method, Sherwood number

Introduction

Many processes in nature as well as engineering rely on mass and heat transfer between a solid surface and an adjacent fluid. Examples are dissolution and crystallization, heterogeneous reactive processes (e.g., combustion of solid fuel, catalysis), and drying. The scalar (heat and/or mass) transfer is due to flow and diffusion. The absence of flow at the very surface (no-slip and no-penetration) makes molecular diffusion the dominant transport mechanism there. Some distance away from the surface, average motion (flow) of the fluid adds to (and often dominates) scalar transfer rates. Flow is generated through the scalar itself (an active scalar and free convection), is imposed by an external mechanism (forced convection with a passive scalar), or is a combination of both (mixed convection).

Engineering design uses mass and heat-transfer correlations for predicting process rates. Such predictions directly relate to overall interfacial area required to achieve design objectives and therefore to estimations of equipment size. In dimensionless form, the correlations are in terms of Sherwood numbers (or Nusselt numbers for heat transfer) as a function of flow conditions and fluid properties via Reynolds and Schmidt numbers (Prandtl numbers for heat transfer) for canonical flow and transfer geometries, for example, flow over plates, through pipes, past spheres, or cylinders. Such correlations have a long and rich tradition and are based on tedious experiments and dimensional analyses.[1–3] Data and correlations have been collected and analyzed in articles and book chapters.[4–6]

The complexity of most practical situations with, for example, dense, dynamic suspensions of solid particles (instead of one sphere in an unbounded domain or a packed bed of monosized spheres), or particles in turbulent flow makes parameterizing the flow with a single Reynolds number challenging and (consequently) yields only coarse, inaccurate scalar transfer predictions. Process designers therefore also rely on experimentation, scale-up studies, and their experience. Numerical simulations are potentially part of their toolbox. The equations to be solved are largely known, and so are the basic material properties (most notably viscosities and diffusion coefficients) and there are many examples of successful applications of numerical solutions to heat and mass transfer problems in fluid-solid systems.[7–9]

Despite successes, challenges in the field of simulation of scalar transfer in solid–liquid suspensions are abundant. They relate to high Schmidt numbers, geometrical complexity, and the presence of a broad range of length scales. Large Schmidt numbers make scalar length scales much smaller than dynamic (flow) length scales so that resolving the scalar field gets a much more demanding task than only resolving the flow field, an issue that has been well recognized in simulations of scalar transfer around bubbles.[10–13] At the length scales of the particles, the interstitial liquid resides in a complexly shaped domain with particles moving relative to one another as moving no-slip boundary conditions. Scalar and particle length scales are in many applications much smaller than the macroscales (e.g., equipment size). In addition,

Correspondence concerning this article should be addressed to J. J. Derksen at jderksen@abdn.ac.uk.

turbulence may add to the complexity by making flows fundamentally three-dimensional (3-D) and extending the spectrum of the scales to be resolved.

It is the aim of this article to contribute to tackling some of the above challenges by suggesting, testing, and applying a numerical procedure for simulating solid-to-liquid scalar transfer at the level of individual moving particles. The procedure is specifically designed for dealing with high Schmidt numbers. Although in this article, we limit ourselves to simulations with one, spherical particle that is allowed to translate and rotate over a fixed grid, extensions to multiple particles are clearly feasible (although not trivial). In part of our simulations, the particle is exposed to a turbulent flow with a Kolmogorov scale typically one order of magnitude smaller than the particle size. This implies that the particle experiences an inhomogeneous hydrodynamic environment and we study the consequences of this for scalar transfer.

The remainder of this article starts with a description of the numerical procedure, where the novel part is the coupled overlapping domain (COD) approach to scalar transport. We then present results for benchmark cases: scalar transfer due to creeping flow and flow at finite Reynolds numbers past a sphere. Subsequently, the sphere is placed in a homogeneous, isotropic turbulent field. Flow, particle motion, and scalar transport are solved simultaneously and fully coupled in a 3-D time-dependent fashion. Conclusions are reiterated and future work is proposed at the end of the article.

Although the terminology in the article is geared toward mass transfer (e.g., Sherwood and Schmidt numbers), the numerical procedure is applicable to forced-convection heat transfer as well.

Numerical Approach

Liquid–solid flow dynamics

In the simulations, a single, solid sphere (radius a, density ρ_p) is placed in a 3-D domain containing a Newtonian fluid (density ρ, kinematic viscosity ν). Usually, the boundary conditions at the edges of the domain are periodic. Throughout this work, the density ratio $\rho_p/\rho = 4$, which is representative for a solid–liquid system. Flow is generated by forcing the fluid and/or the particle. In the benchmark simulations, a uniform body force creates a laminar flow past the sphere. In the turbulence simulations, linear forcing[14] generates homogeneous, isotropic turbulence (HIT) with a preset power supply per unit liquid mass. The simulations fully resolve the turbulence [direct numerical simulations (DNS)]. The motion of the fluid and the particle are two-way coupled, that is, the particle moves under the influence of hydrodynamic forces; conversely, the fluid feels the translational and rotational motion of the particle through the no-slip and no-penetration conditions at the sphere's surface. In many of the benchmark simulations, the sphere is held in a fixed location.

The lattice-Boltzmann (LB) method,[15,16] supplemented with an immersed boundary (IB) approach[17] to enforce no-slip and no-penetration at the sphere surface, is used to evolve the flow system in time. The IB method provides the hydrodynamic force and torque on the sphere that are used to update the sphere's linear and angular velocity and position. The flow is solved on a uniform, cubic grid and (if the sphere is mobile) the sphere moves over this grid. The default resolution is such that the sphere radius spans eight grid spacings: $a = 8\Delta$. Excursions to $a = 12\Delta$ and 16Δ have been undertaken to assess grid effects. In the turbulence simulations, the Kolmogorov scale typically is $\eta_K \approx \Delta$. This numerical approach, including turbulence generation, hydrodynamic radius calibration, and resolution tests has been documented in previous articles of ours.[18,19]

Scalar transport

To study solid–liquid scalar transfer, a passive scalar with concentration $c(\mathbf{x}, t)$ is introduced in the liquid. Its transport equation reads

$$\frac{\partial c}{\partial t} + \mathbf{u} \cdot \nabla c = \Gamma \nabla^2 c \tag{1}$$

with $\mathbf{u}$ the liquid velocity field, and Γ the scalar diffusivity. The Schmidt number is recognized as $\mathrm{Sc} \equiv \nu/\Gamma$. A boundary condition $c = 1$ is imposed at the surface of the solid sphere. This boundary condition implies that in this study, we do not consider transfer processes inside the particle (such as intraparticle heat transport). The particle radius a does not depend on time, that is, we do not simulate a dissolution process.

The scalar transport simulations usually start with a fully developed flow and $c = 0$ everywhere in the liquid. At time zero we start solving Eq. 1, including its $c = 1$ boundary condition, and we keep solving the flow equations. Starting from $t = 0$, solid-to-liquid transfer is monitored by keeping track of

$$\dot{m} = -\Gamma \int_A \frac{\partial c}{\partial n} dA \tag{2}$$

with A the surface of the sphere, n the normal to the surface pointing into the liquid, and $\dot{m}$ the scalar flux. Usually, the scalar flux is parameterized by a transfer coefficient k: $\dot{m} = kS\Delta c$. In this case, the overall concentration difference is $\Delta c = 1$, and the surface area is $S = 4\pi a^2$. We then have $k = \dot{m}/(4\pi a^2)$ and $\mathrm{Sh} \equiv \frac{k2a}{\Gamma} = \frac{\dot{m}}{2\pi\Gamma a}$ with Sh the Sherwood number.

Our interest in liquid systems implies that Schmidt numbers $\mathrm{Sc} \gg 1$, and strong concentration gradients are to be expected near the particle surface. As these gradients eventually determine the scalar transfer process (see Eq. 2), proper spatial resolution of the scalar field close to the surface is essential for good Sherwood number predictions.

Coupled overlapping domains

Given that $\mathrm{Sc} \gg 1$, the cubic grid with a resolution of typically $\Delta = a/8$ that serves well in resolving the flow dynamics,[18,19] will not be able to sufficiently resolve the scalar field. At the same time, we recognize that scalar resolution challenges are largely confined to a region close to the sphere. We therefore propose to solve the scalar transport equation (Eq. 1) on two coupled overlapping domains (COD). This is illustrated in Figure 1. The outer domain has the same cubic grid as the LB solver. The inner domain is a spherical shell with inner radius a and thickness δ. It has been discretized by a grid along the spherical coordinates (r, θ, φ): $a \le r \le a+\delta$, $0 \le \theta \le \pi$, and $0 \le \varphi \le 2\pi$ with θ running from pole to pole and $\theta = \pi/2$ on the equator. For simplicity, radial and angular steps (Δr, $\Delta\theta$, $\Delta\varphi$) are uniform. Also for simplicity, it was decided not to discretize the shell with a "cubed sphere approach."[20] An advantage of the latter would be avoiding the anisotropy that is inherent to spherical grids with meridians clustering near the poles. It

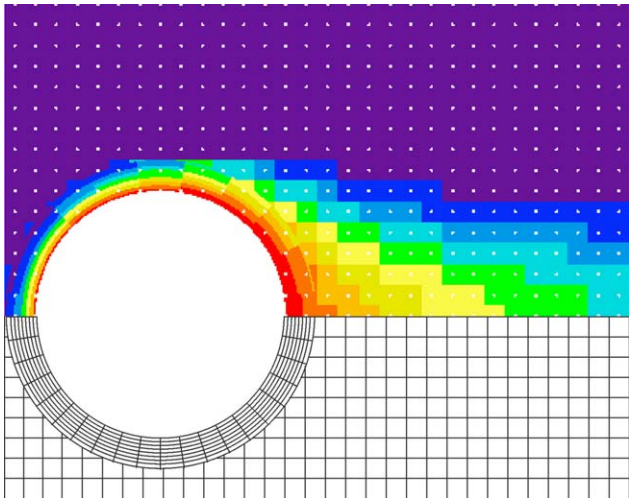

Figure 1. Impression of COD.

A spherical shell with a grid in spherical coordinates interacts with an outer uniform cubic grid. [Color figure can be viewed in the online issue, which is available at wileyonlinelibrary.com.]

will be demonstrated later in the article, however, that—with sufficient angular resolution—the scalar transfer results are insensitive to the way the spherical grid is oriented relative to the outer grid.

On the outer domain, Eq. 1 is solved by an explicit finite volume (FV) scheme with total variation diminishing (TVD) discretization with the superbee flux limiter for the convective fluxes.[21–23] The latter suppresses numerical diffusion. This way of dealing with scalar transport in a flow field generated by the LB method has been utilized in many of our previous articles, the first one being Ref. 24.

An FV scheme is also used for solving Eq. 1 on the spherical grid in the shell around the sphere. In this scheme, time stepping has been done in a mixed implicit/explicit way: the focusing of grid lines near the poles makes that for stability reasons we need to treat the φ derivatives implicitly. With the explicit treatment of the r and θ derivatives, we avoid solving large linear systems of equations and instead deal with solving multiple tridiagonal systems each time step. For the convective fluxes, central differences have been applied in the angular directions; the same TVD scheme as noted

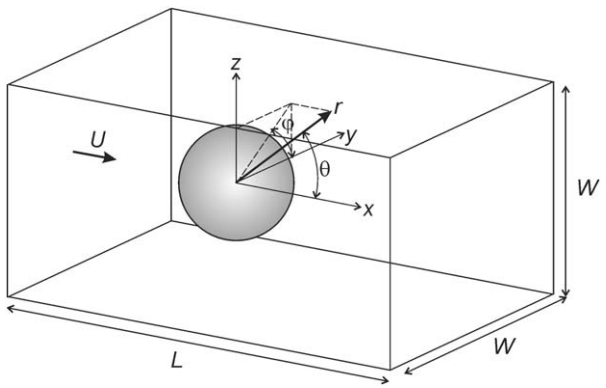

Figure 2. Benchmark configuration for the flow past a sphere in a rectangular domain.

The origins of the Cartesian and spherical coordinate system coincide with the center of the sphere.

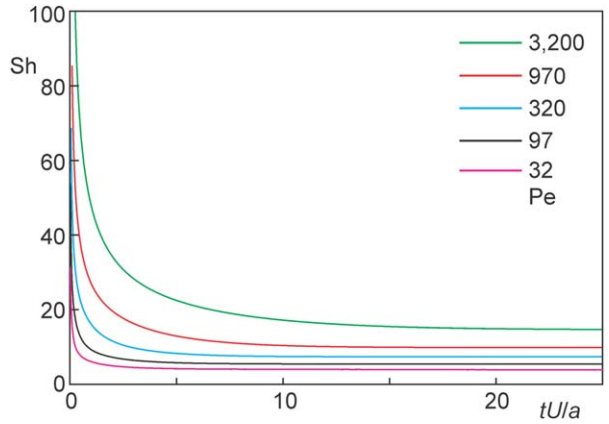

Figure 3. Evolution of the scalar transfer process for creeping flow past a sphere.

Sherwood number as a function of dimensionless time for a range of Peclet numbers. [Color figure can be viewed in the online issue, which is available at wileyonlinelibrary.com.]

above has been used in the radial direction. In this study, concentration is imposed at the solid surfaces (Dirichlet boundary conditions). If desired, the numerical approach allows in a straightforward manner for gradient (Neumann) or mixed conditions. Unless very steep gradients are imposed through a Neumann condition, the presently used Dirichlet condition is the most challenging in terms of spatial resolution.

The spherical grid is attached to the sphere, and Eq. 1 is solved in a reference frame moving (translating and rotating) with the sphere. The spherical grid itself has a fixed orientation with the line connecting the poles aligned with one of the Cartesian coordinate directions. The relative velocity field in the shell is denoted by $\mathbf{v}(r, \theta, \varphi; t)$, the velocities in the outer domain with the cubic grid in a fixed frame of reference by $\mathbf{u}(x, y, z; t)$.

The two (cubic and spherical) grids communicate through interpolation of velocity as well as concentration fields. The velocity field on the spherical grid is imposed by the LB solution $\mathbf{u}$. For reasons to be discussed below, the shell thickness δ is comparable to the cubic grid spacing Δ (typically $\delta/\Delta \approx 1$ to 3). The radial spacing in the spherical grid is much smaller than Δ (of the order of $\Delta r \approx 0.1\Delta$) so that (at least in radial direction) we need to interpolate from a coarse $\mathbf{u}$ field to a fine $\mathbf{v}$ field. This is done as follows: for each discrete $\theta^{(j)}$, $\varphi^{(k)}$ angular location, the velocity relative to the sphere at three radial positions is determined: At $r = a$, $\mathbf{v} = \mathbf{0}$ by definition; at $r = a + \delta/2$ and $r = a + \delta$, $\mathbf{v}$ is determined through linear interpolation from the known velocities $\mathbf{u}$ on the cubic grid, and the known velocity (linear and angular) of the sphere $\mathbf{v_p}$, $\mathbf{\Omega_p}$. These velocity support points at three radial locations are connected through a (unique) quadratic function of r that is used to determine the velocities at each discrete radial location $\mathbf{v}(r^{(i)}, \theta^{(j)}, \varphi^{(k)}; t)$ on the spherical grid. Because the three velocity support points are a distance of order Δ apart, we do not over or under interpolate the LB velocity field $\mathbf{u}$ to the spherical grid. The spherical velocity field has a staggered arrangement, that is, velocities are located at the faces of cells so as to simplify the FV implementation. The velocity fields on cubic and spherical grid are to a very good approximation incompressible. Some of the choices made in the above

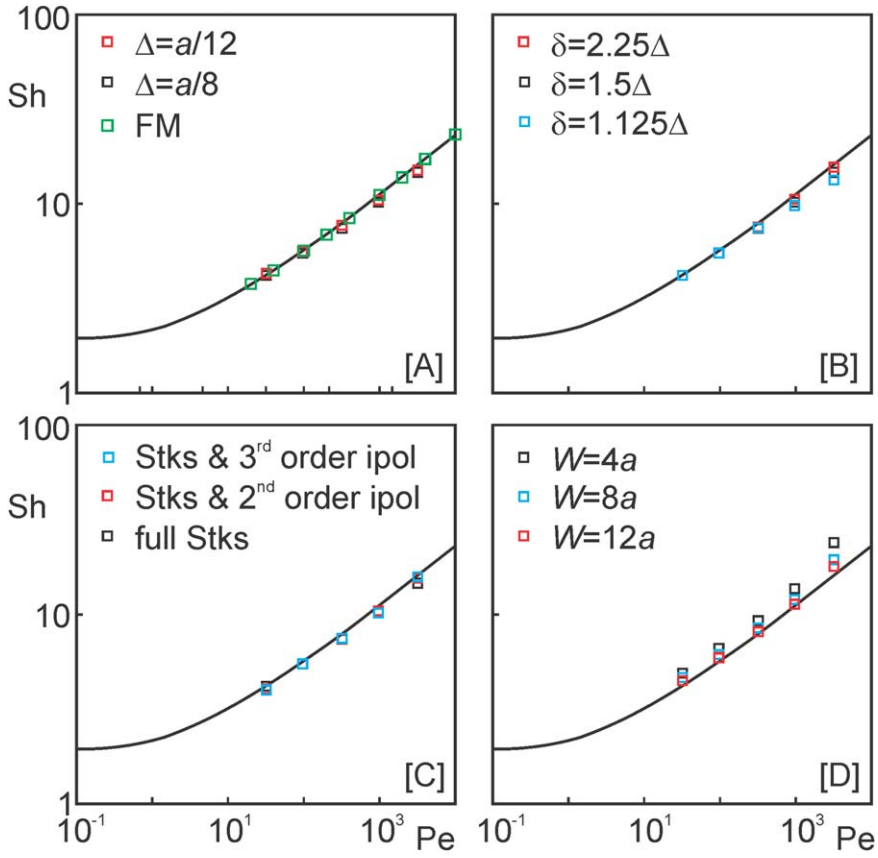

Figure 4. Steady state Sherwood number as a function of Peclet number for creeping flow past a sphere.

The drawn curve (same in all four panels) is from Ref. 6. A: Effect of resolution Δ with Stokes' solution for the flow, plus reference data (FM).[27] B: Effect of shell thickness δ with Stokes' solution for the flow. C: Results with Stokes' solution on both grids ("full") and Stokes' solution on the cubic grid and an interpolated (second-order and third-order) flow field on the spherical shell grid. D: Results with LB flow solution with periodic boundary conditions, effects of domain width W. [Color figure can be viewed in the online issue, which is available at wileyonlinelibrary.com.]

procedure (e.g., quadratic interpolation and the locations of the support points) have been checked through sensitivity tests.

In the time stepping process, the concentration field on the cubic grid serves as a boundary condition for the concentration field on the spherical grid, and vice versa: at the start of each time step, the concentration field at the edge of the spherical shell (i.e., at $r = a + \delta$) is determined through linear interpolation from the concentration solution on the cubic grid at the old time level. Then, the concentration field in the spherical shell is updated which can be done because we have known concentrations at its radial edges $r = a$ ($c = 1$) and $r = a + \delta$ (interpolated). For spherical grids with fine Δr, this shell update may consist of multiple subtime-steps for reasons of stability (i.e., to keep $\Delta t < \frac{1}{2}\frac{\Delta r^2}{\Gamma}$). After the shell concentration update, nodes on the cubic grid that are covered by the shell get assigned a new concentration value that is linearly interpolated from the new time level solution on the spherical grid. These nodes of the cubic grid are not touched anymore in the cubic grid concentration update that now follows. In fact, the cubic grid nodes covered by the shell near the outer edges of the shell serve as boundary values for the concentration update on the cubic grid. This cubic grid update completes one scalar time step on the spherical as well as on the cubic grid.

It should be noted that the sphere is allowed to move relative to the cubic grid. The shell is attached to the sphere, and the concentrations on nodes inside the shell (including those that reside on the cubic grid) are governed by the concentration field on the spherical grid. This implies that our COD approach does not require a "refill" procedure (such as e.g., used in LB context[25]) for cubic grid nodes that get uncovered by the moving sphere. Cubic grid nodes that get uncovered by the shell already have a (physically sound) concentration attached to them based on the former concentration field in the shell.

An important choice to be made is for the shell thickness δ. It has to be larger than the cubic grid spacing Δ so as to have at least one layer of cubic grid points around the sphere that fall in the shell and thus can serve as boundary conditions for a cubic concentration field update. The shell also should not be unnecessarily thick. It has no function beyond resolving the concentration boundary layer and making it much thicker would be computationally inefficient. In addition in future work, we want to go beyond a single sphere and plan to study scalar transfer in dense solid–liquid suspensions. We then unavoidably will be dealing with overlapping shells. This likely will require some level of modeling (as opposed to directly solving the transport equations) with regards to mixing of concentrations in overlapping shells. To simplify such modeling and minimize the impact of the modeling steps, thin shells, and thus small shell overlap volumes are to be preferred.

In this work, the default shell thickness is set at $\delta = 1.5\Delta$ and the sensitivity to this choice is investigated.

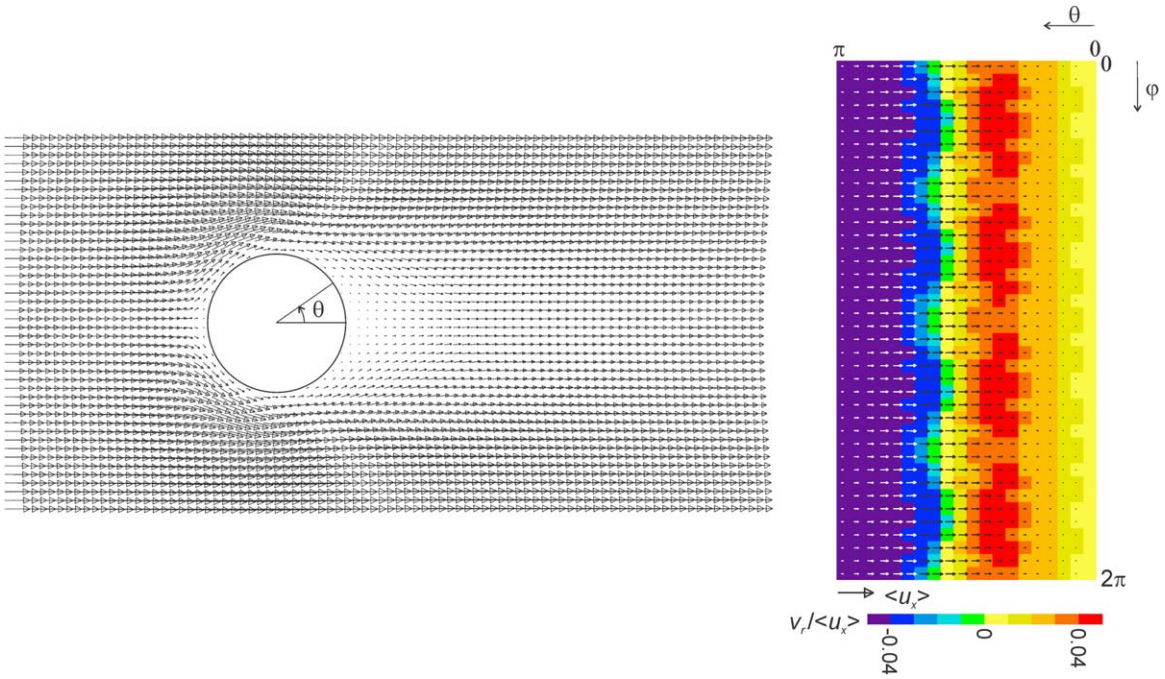

Figure 5. Flow past a sphere at Re = 22.3.

Left: velocity vectors on the cubic grid in the *xz* plane through the center of the sphere (note that this panel shows only part of the overall flow domain). Right: velocity field in the spherical shell at $r=a+\delta/2$; the color contours indicate radial velocity; the vectors are the velocity parallel to the sphere surface. The reference velocity $\langle u_x \rangle$ is the average *x*-velocity in the fluid volume. [Color figure can be viewed in the online issue, which is available at wileyonlinelibrary.com.]

Benchmarks

To verify and validate our simulation procedure, and to check sensitivities to numerical parameters, scalar transfer due to the flow past a single, rigid sphere is considered. We distinguish between two different situations: creeping flow and steady laminar flow at finite Reynolds numbers, with $\mathrm{Re} \equiv U2a/\nu$ and U a relevant velocity scale. The availability of Stokes' solution for creeping flow past a sphere[5] allows us to assess the performance of the scalar solver independent of the (LB) flow solver. For some of the finite Reynolds number cases, we compare scalar transfer rates at static spheres with those at spheres moving relative to the cubic grid.

The reference data we use can be found in the seminal book by Clift, et al.[6] Their Figure 3.10 shows (amongst more) the Sherwood number as a function of the Peclet number $\mathrm{Pe} \equiv U2a/\Gamma$ for creeping flow. The correlation

$$\mathrm{Sh} = 1 + \left[1 + \left(\frac{1}{\mathrm{Pe}}\right)\right]^{1/3} \mathrm{Pe}^{0.41}\,\mathrm{Sc}^{-0.08} \tag{3}$$

(rewritten from Eq. 5–25 in Ref. 6) is used for comparison with finite Reynolds number results. It has been reported[6] that Eq. 3 is within 3% accuracy for $1 < \mathrm{Re} < 400$ and $0.25 < \mathrm{Sc} < 100$.

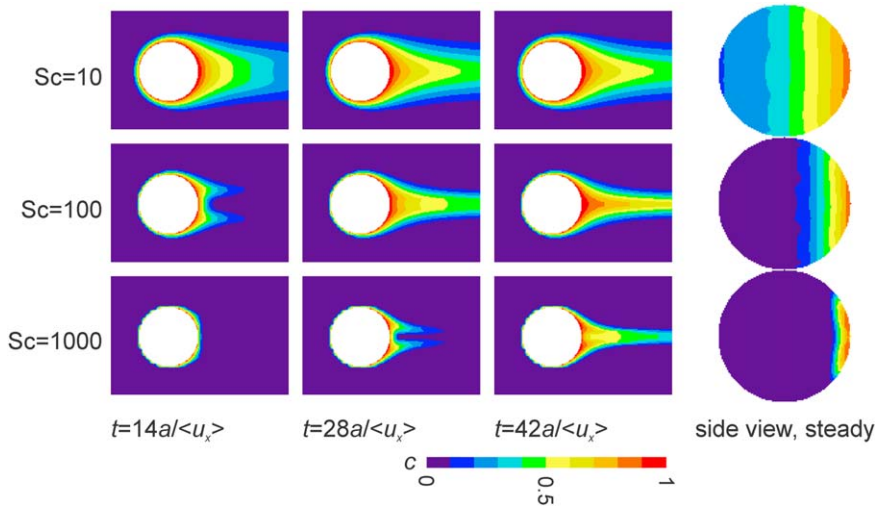

Figure 6. Scalar transfer for the flow past a sphere at Re = 22.3.

Scalar concentration in the *xz*-plane through the center of the sphere on the cubic grid for different Sc (top to bottom) and time (left to right). Far right: side view of the concentration on the outer surface of the shell ($r = a + \delta$) after steady state is reached. [Color figure can be viewed in the online issue, which is available at wileyonlinelibrary.com.]

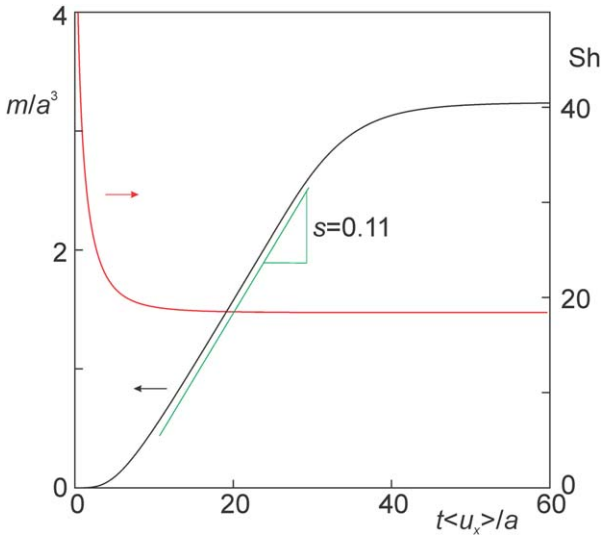

Figure 7. Time series of the total amount of scalar (m) on the cubic grid outside the shell and of the Sherwood number for flow past a sphere at Re = 22.3 and Sc = 100.

The green line indicates the slope of portion of the m time series. [Color figure can be viewed in the online issue, which is available at wileyonlinelibrary.com.]

Creeping flow past a sphere

A fixed sphere of radius a is placed in a rectangular domain of size $L\times W\times W$, see Figure 2. The figure defines a Cartesian and a spherical coordinate system that both have their origin in the sphere center. Overall flow is in the positive x-direction. The default domain size is $L/a = 8$ and $W/a = 4$; the center of the sphere is a distance $L/4$ from the inlet plane and in the middle of the domain in y and z direction. In the domain, the liquid velocity according to Stokes' solution for creeping flow around the sphere with free stream velocity U is imposed

$$v_r = U\cos\theta\left(1+\frac{r^3}{2a^3}-\frac{3r}{2a}\right),$$
$$v_\theta = U\sin\theta\left(1-\frac{r^3}{4a^3}-\frac{3r}{4a}\right), \quad v_\varphi = 0 \tag{4}$$

Equation 4 is discretized on the cubic grid with spacing $\Delta = a/8$ that covers the entire domain, and on a spherical grid in a shell around the sphere with thickness $\delta = 1.5\Delta$. Spacings in the spherical grid are $\Delta r = \delta/16$ and $\Delta\theta = \Delta\varphi = \pi/20$. This velocity field and these grids are used for solving the scalar transport equation (Eq. 1). Concentration boundary conditions are $c = 1$ at $r = a$, $\frac{\partial c}{\partial x} = 0$ at the inlet and outlet planes, and periodic conditions along the other boundaries. Initially $c = 0$ everywhere in the liquid. The diffusivity is set such as to achieve five Peclet numbers: Pe = 32, 97, 320, 970, and 3200, respectively.

Resolution requirements in radial direction can be estimated as follows. A time scale for the flow past the sphere is a/U. During this time, the scalar diffuses over a distance relative to the sphere radius of typically $\frac{\sqrt{\pi\Gamma a/U}}{a} = \sqrt{\frac{\pi}{\mathrm{Pe}}}$. The radial grid should be well able to resolve this diffusion layer: $\frac{\Delta r}{a} < \sqrt{\frac{\pi}{\mathrm{Pe}}}$. For the highest Peclet number of 32,000, $\sqrt{\pi/\mathrm{Pe}} \approx 0.03$ whereas $\Delta r/a \approx 0.006$.

Starting from the initial condition, the simulations keep track of the Sherwood number as a function of time. It is determined by numerically performing the differentiation and integration in Eq. 2. Results for the five Peclet numbers are given in Figure 3. Initially, scalar transfer is very strong due to fresh fluid getting in contact with the sphere surface. In the course of time, a scalar boundary layer establishes itself around the sphere and a steady state sets in after a time of the order of 10 a/U. In accordance to a criterion introduced earlier,[26] the Sherwood time series are assumed to have reached steady state if the change in Sh during the last 20% of the computational time was less than 1%. These steady state Sherwood numbers are compared with the results given in Clift, et al,[6] see Figure 4A. For further reference, Figure 4A also contains data from Feng and Michaelides.[27] Good agreement with a slight underestimation (up to 9%) of Sherwood numbers at higher Pe is observed. The underestimation is not a result of an insufficiently fine grid in radial direction. A refinement by a factor of 2 ($\Delta r = \delta/32$) results in virtually the same steady state Sherwood numbers (differences less than 0.2%, not shown in Figure 4). A finer cubic grid with $\Delta = a/12$ improves the agreement with the reference data to deviations of up to 6% (see Figure 4A). In Figure 4B, the impact of the choice of the shell thickness is detailed, with the thinner shell of $\delta = 1.125\Delta$ performing not as well as the default and thicker shell.

To test the interpolation of the velocity field to the spherical grid (as outlined above), simulations are also performed in which the Stokes solution is only applied to the outer, cubic grid, and the velocity field on the spherical grid is interpolated with a quadratic function (the default), and also (for assessing sensitivity) with a third-order polynomial (on four radial support points). The differences in terms of

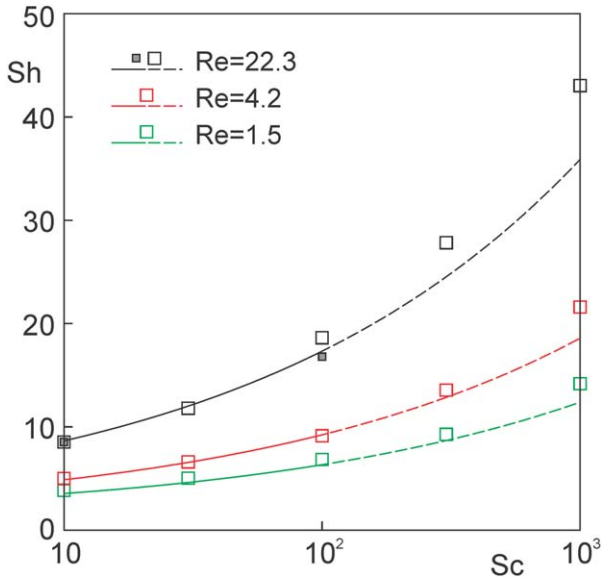

Figure 8. Sherwood number as a function of Schmidt number for flow past a sphere at three Reynolds numbers as indicated.

Line: correlation (Eq. 3) where the transition from solid to dashed indicates that Eq. 3 is accurate up to Sc = 100. Open symbols are simulation results with default numerical and geometrical settings. The two closed symbols are benchmark data from Ref. 28 at Re = 20. [Color figure can be viewed in the online issue, which is available at wileyonlinelibrary.com.]

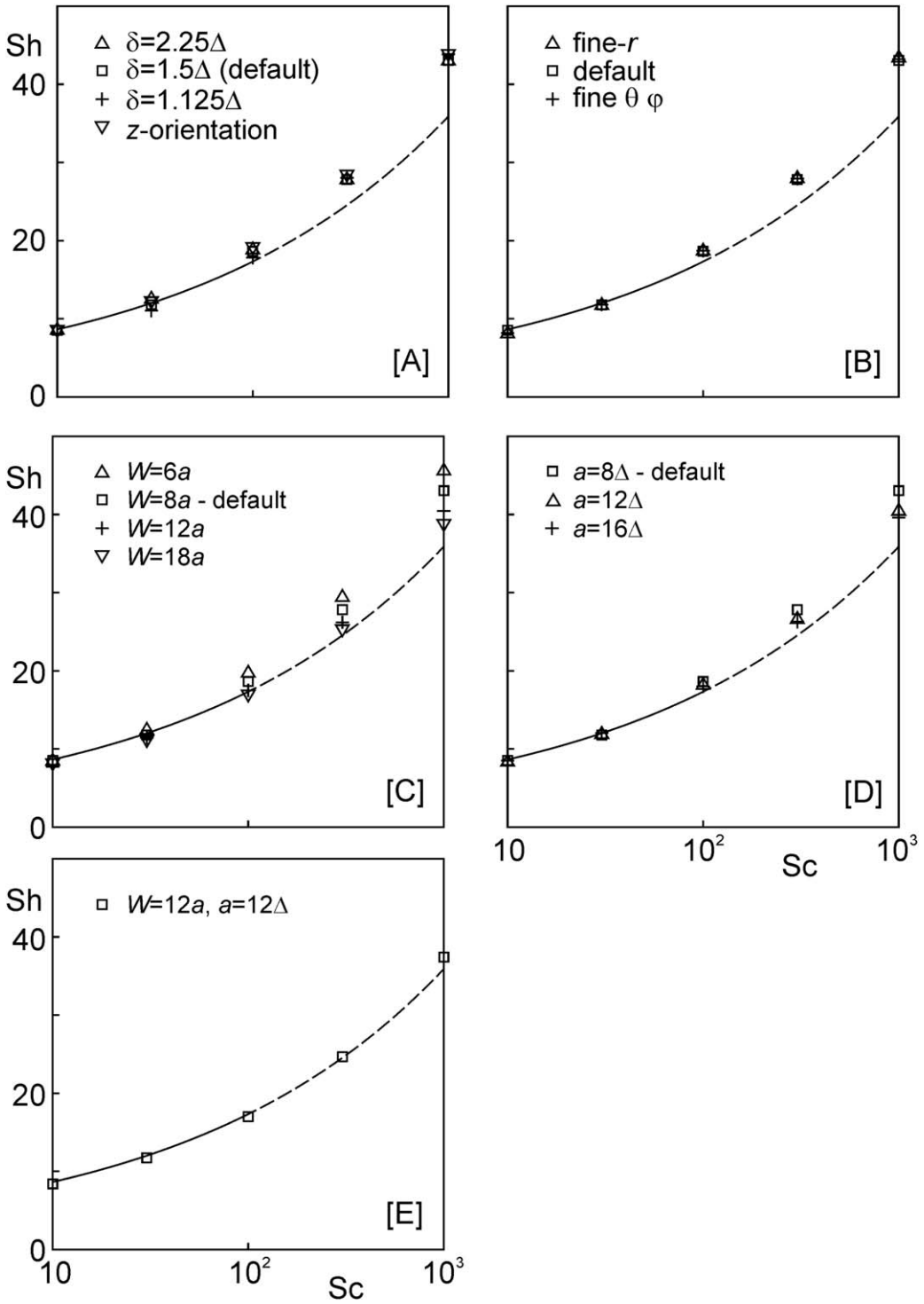

Figure 9. Dependencies of the Sh-Sc relationship at Re = 22.3 for various numerical and geometrical variables.

A: Effect of shell thickness $\delta$and spherical grid orientation relative to flow direction. B: Effect of spherical grid resolution; fine-r has twice as small Δr as default; fine $\theta\varphi$ twice as small $\Delta\theta$ and $\Delta\varphi$. C: Effects of system size dimension W. D: Effects of the resolution of the cubic grid. E: Combined effect of cubic grid refinement and increased domain size.

Sherwood numbers in Figure 4C between "full Stokes" (Stokes on outer and inner grid), and second-order and third-order velocity interpolation are marginal, providing confidence in the velocity interpolation procedure.

As a next step, instead of using Stokes' solution for velocity, a LB solution at low Reynolds number (Re = 0.05), and quadratic velocity interpolation to the spherical grid are used to solve the scalar transport equation. For obtaining the LB solution, fully periodic conditions and a domain with dimensions $L/a = 8$ and $W/a = 4$ are applied. Therefore, the flow boundary conditions are different from the (at infinity) boundary conditions leading to the Stokes solution; the former conditions essentially mimic a regular, 3-D array of spheres through which liquid is forced. These LB flow results lead to a clear overestimation of the Sherwood number, see Figure 4D. The finite domain size in conjunction

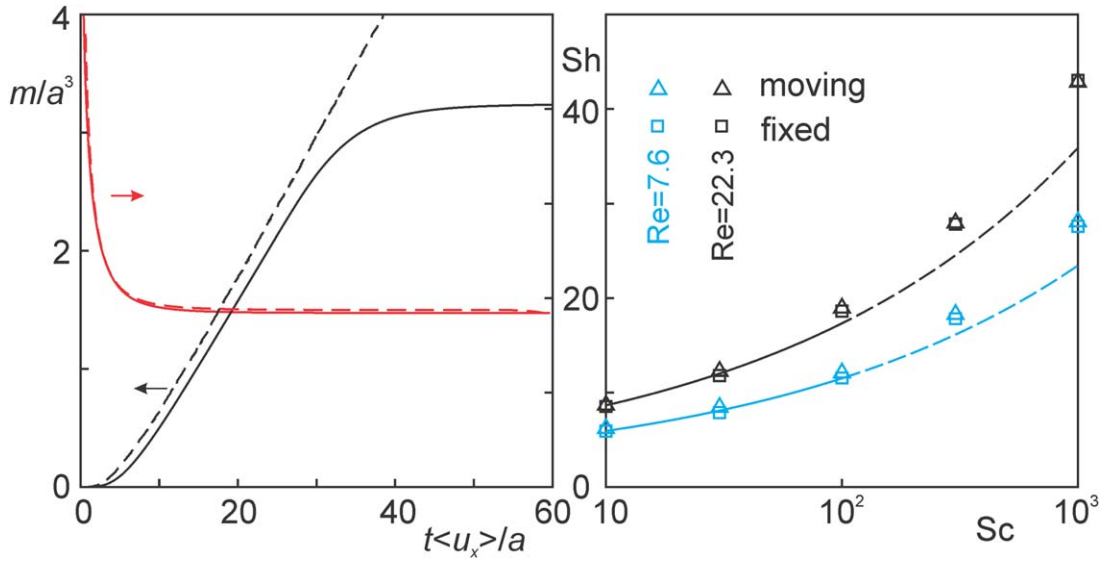

Figure 10. Comparison between a fixed and a moving sphere.

Left: time series of total amount of scalar in the fluid and Sh at Re = 22.3 and Sc = 100. Solid curves: fixed sphere (same data as Figure 7); dashed curves: moving sphere. Right: steady state Sherwood numbers as a function of Sc for Re = 7.6 and 22.3. [Color figure can be viewed in the online issue, which is available at wileyonlinelibrary.com.]

with the periodicity of the flow boundary conditions are largely the reason for this overestimation; an increase of the width W of the domain strongly reduces the deviation from the reference data, see again Figure 4D.

Scalar transport for flow past a sphere at finite Re

A configuration as in Figure 2 was also used to study flow and scalar transport at finite Reynolds numbers. The flow is driven by a uniform body force on the fluid in the x-direction, which was controlled in such a way as to achieve a desired Reynolds number that now is based on the volume-averaged velocity in x-direction: $\mathrm{Re}=\langle u_x\rangle 2a/\nu$. By default the domain size is $L/a = 16$ and $W/a = 8$; the resolution of the cubic grid is $\Delta = a/8$. The case with $\mathrm{Re} = 22.3$ is used as a reference case, that is, its sensitivity for numerical choices is studied, specifically in terms of the Sherwood number.

Impressions of the LB solution for the flow at the reference Reynolds number are given in Figure 5. The fore-aft asymmetry is clear from the xz cross section. At this Reynolds number, there is no recirculating wake; recirculation for a sphere placed in uniform flow typically sets in at $\mathrm{Re} \geq 37$.[6] The velocity field on the cubic grid was interpolated to a grid in a spherical shell with thickness $\delta = 1.5\Delta$, and $\Delta r = \delta/16$ and $\Delta\theta = \Delta\varphi = \pi/20$. Figure 5 also shows the velocity field in the spherical shell. The acceleration and then deceleration of liquid moving past the sphere is clearly observed through the vectors in the (θ, φ)-view. The contours in the (θ, φ)-view show that radial velocities are negative (transport toward the sphere surface) for $\theta \geq 0.6\pi$ and positive for smaller angles θ. The velocity contours show some scatter with a four-fold symmetry which is due to the interpolation from the cubic grid on the spherical shell. The scatter in this plot is enhanced by showing the contours with the resolution of the angular grid, hence the block-like structure of the contour plot.

The scalar transport equation (Eq. 1) is solved with this velocity field for five values of the Schmidt number: 10, 30, 100, 300, and 1000. As for the creeping flow benchmark, the concentration on the sphere is set to $c = 1$; $\frac{\partial c}{\partial x} = 0$ at the inlet and outlet planes; periodic conditions apply along the other outer boundaries.

The scalar transfer from the solid surface to the liquid is highly sensitive to the Schmidt number, as demonstrated in Figure 6 that shows concentration fields at different moments in time and on the two grids. The zero-gradient conditions for scalar transport on the upstream and downstream boundary allow for the existence of a steady concentration field where the rate at which the scalar enters the liquid through diffusion at the sphere's surface is balanced by the removal through the exit plane. Well before this overall steady concentration state is reached, however, the transfer rate at the sphere's surface has become virtually steady, see Figure 7 that shows time series of the Sherwood number as determined through Eq. 2, and the total scalar mass m on the cubic grid, outside the shell. After a time period of $t \approx 10a/\langle u_x\rangle$, m increases linearly, so that $\dot{m}$ is constant in time. At $t \approx 30a/\langle u_x\rangle$, m levels off. From then on scalar is present at the exit boundary and leaves the domain. Next to via Eq. 2, the Sherwood number can thus be determined through the slope s in Figure 7. With the scaling of the axes as used in Figure 7 $\mathrm{Sh} = \frac{s}{4\pi}\mathrm{Pe}$; for $s = 0.11$ and $\mathrm{Pe} = 2.23\cdot 10^3$ this results in $\mathrm{Sh} = 19.5$. The average Sherwood number based on Eq. 2 in the time period $15a/\langle u_x\rangle \leq t \leq 25a/\langle u_x\rangle$ (i.e., the "most linear" part of the m vs. t curve) is $\mathrm{Sh} = 18.7$, that is, 4% lower. This is an indication for the level of consistency of the communication (through linear interpolation) between the two coupled, overlapping grids because one Sherwood estimate (via Eq. 2) is determined on the inner grid and the other (via the m-slope) on the outer grid.

In Figure 8, an overview of results for the Sherwood number as a function of Reynolds and Schmidt number is presented and compared to the correlation in Eq. 3. These results are obtained with the default domain size and resolutions on the two grids as defined above. For reference, Figure 8 also contains two data points from the literature[28] at $\mathrm{Re} = 20$. Up to $\mathrm{Sc} = 100$, the deviations between simulations and correlation are within 8%, beyond $\mathrm{Sc} = 100$ the deviations significantly increase, to an overestimation by 18% at

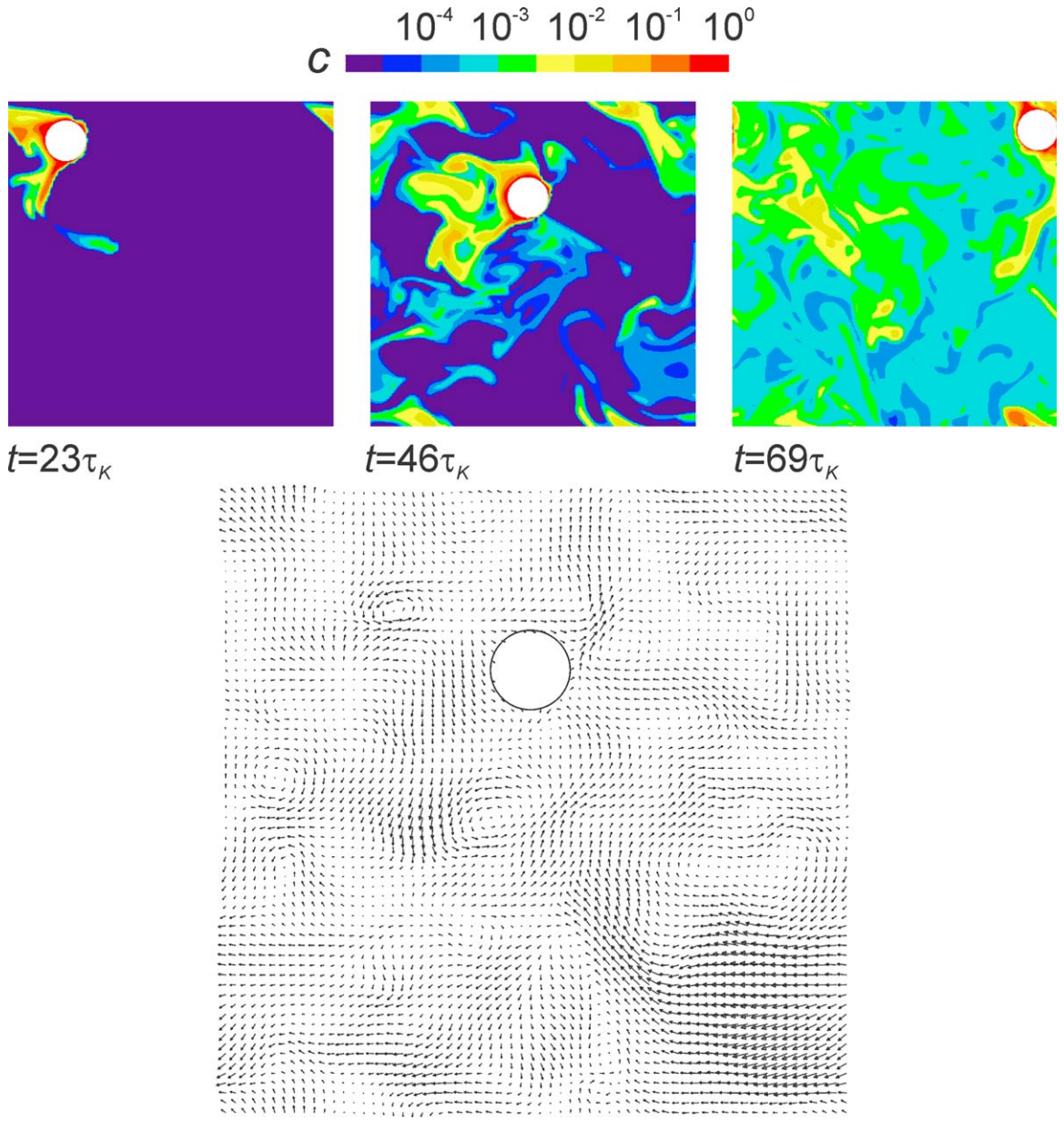

Figure 11. Cross sections in planes through the center of the sphere of realizations of the scalar concentration field (top, Sc = 100) and velocity field for the turbulent case with $a/\eta_K = 10.7$.

The moment of the vector field is the same as for the middle concentration panel ($t=46\tau_K$). The resolution of the cubic grid is twice as high (in each dimension) as the density of the velocity vectors. [Color figure can be viewed in the online issue, which is available at wileyonlinelibrary.com.]

Sc = 1000 and Re = 22.3 where it should be noted that the correlation (Eq. 3) is recommended only for use up to Sc = 100 [6].

For the highest Reynolds number in Figure 8, that has the strongest deviations, geometrical and grid effects are checked. Results of these exercises are presented in Figure 9. The characteristics of the spherical shell and its grid are of minor influence on Sh. Changing the shell thickness δ causes small changes in the Sherwood number, the more remarkable one being a decrease of Sh at Sc = 30 upon reduction of δ, see Figure 9A. As an aside, Figure 9A also shows the effect of change in orientation of the spherical grid relative to the flow. By default the line connecting the poles of the spherical grid is aligned with the x (is flow) direction. The consequences for changing this to the z-direction (and further default conditions) are minor. The same can be said for refining the spherical grid, see Figure 9B. In terms of the radial grid this is understood based on the earlier noted demand for resolution: with the highest $\mathrm{Pe}=\mathrm{Sc}\,\mathrm{Re}=2.23\cdot 10^4$, $\sqrt{\pi/\mathrm{Pe}} \approx 0.012 > \Delta r/a \approx 0.006$ with the latter the (default) radial resolution.

The overall size of the rectangular flow domain and the resolution of the cubic grid are major factors in the deviations between simulations and correlation, see Figures 9C, D. In Figure 9C, the domain size is varied in the lateral directions (W/a in the range 6–18, with 8 the default). An increase in W reduces the Sherwood number which can be understood by the periodic flow conditions. In narrow domains, the liquid has to squeeze through closely spaced spheres in a periodic arrangement which enhances scalar transfer. Because the enhancement is flow-related, it is

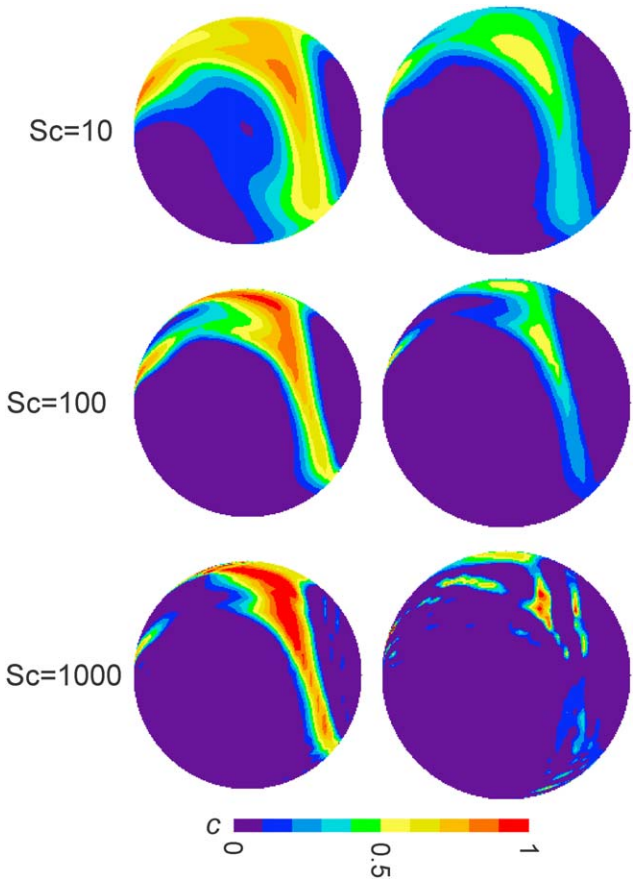

Figure 12. Side views of instantaneous realizations of scalar concentration in the spherical shell at $r=a+\delta/2$ (left) and $r=a+\delta$ for three Schmidt numbers.

Turbulent conditions with $a/\eta_K = 10.7$. All six panels are at the same instant in time. [Color figure can be viewed in the online issue, which is available at wileyonlinelibrary.com.]

stronger for higher Sc for which flow (as compared to diffusion) is more important for scalar transfer.

A subtle point in this discussion is the definition of the Reynolds number $\mathrm{Re}=\langle u_x\rangle 2a/\nu$ with $\langle u_x\rangle$ the volume-averaged x-velocity. In wider domains, the relative influence of the low velocity region near the sphere on the average velocity is smaller so that a Reynolds number based on a free-stream velocity would decrease for flows in wider domains having the same average velocity. To quantify this effect, Reynolds numbers based on an x-velocity in a point far away from the sphere (we took that point in the corner of the domain, all eight corners are the same given the periodic conditions) are determined as estimates for free-stream Reynolds numbers. These Reynolds number are within 1% for all cases in Figure 9C, which—given Eq. 3—cannot account for the variability of some 20% in the Sherwood number with domain width for Sc = 1000.

Resolution of the cubic grid also has its effect on the Sherwood number. In Figure 9D, a comparison between $a=8\Delta$, 12Δ, and 16Δ is presented where all further dimensions relative to a were kept constant. For Sc = 1000 the Sherwood numbers are Sh = 43.7, 40.4, and 39.7, respectively, and thus tend to converge. According to Eq. 3, the Sherwood number should be Sh = 35.9. Finally, the combined effect of domain size and cubic-grid resolution is assessed in Figure 9E where deviations between simulation and correlation are less than 5% over the full range of Schmidt numbers.

So far the sphere is at a fixed location with liquid flow past it. The numerical procedure is designed, however, to allow for a sphere moving relative to the cubic grid. For this reason, we designed simulations where a single sphere was settling steadily in a fully periodic domain at Re = 22.3 and 7.6 with $\mathrm{Re}=|v_{px}-\langle u_x\rangle|2a/\nu$ and v_{px} the x-component of the velocity of the sphere. Different from the static-sphere cases above, the scalar boundary conditions now need to be fully (3-D) periodic. To delay the moment scalar from the wake reaches the front of the sphere, the domain is made longer than for the static sphere, $L/a = 40$. The rest of the aspect ratios are the same as for the default static sphere. The results of the moving-sphere cases are summarized in Figure 10. The evolution of m and Sh is directly compared to its fixed-sphere counterpart in Figure 10A. The longer domain and periodic scalar conditions for the moving sphere make that the m-curve does not level off within the time window of the figure; its slope, however, is very close to that of the static sphere. Careful observation shows some fluctuations in the m-curve of the moving sphere which are due to the motion of the sphere plus shell over the cubic grid. The Sherwood numbers for moving and static sphere are very

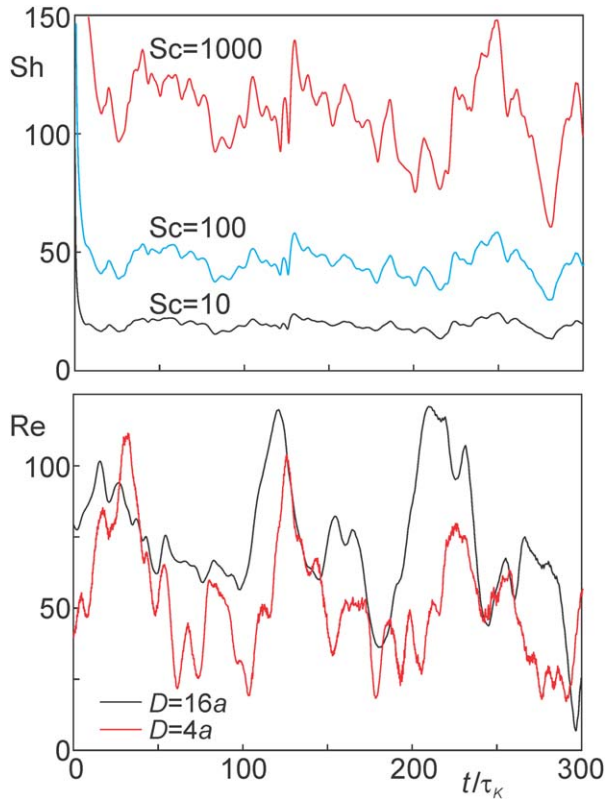

Figure 13. Top: times series of the Sherwood number under turbulent conditions (at $a/\eta_K = 10.7$) for three Schmidt numbers.

Bottom: particle Reynolds numbers based on the slip velocity $|v_p-\langle u\rangle|$ with the volume averaged liquid velocity $\langle u\rangle$ taken over a cubic volume D^3 centered around the particle. Default numerical settings. [Color figure can be viewed in the online issue, which is available at wileyonlinelibrary.com.]

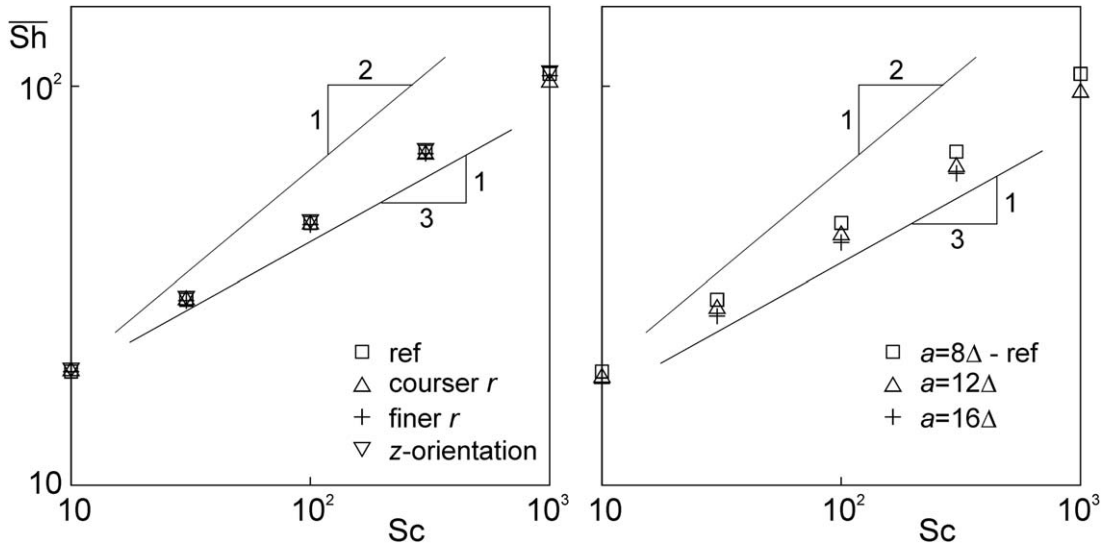

Figure 14. Time-averaged Sherwood number vs. Sc for a sphere in turbulent flow with $a/\eta_K = 10.7$.

Effects of grid resolution. Left: comparison between the reference case and spherical grids that are courser and finer (by a factor of 2) in the radial direction; *z*-orientation refers to a sphere with the line connecting the poles in *z*-direction instead of (default) *x*. Right: effects of cubic grid resolution as defined by the number of grid spacings spanning sphere radius *a*. The 1/2 and 1/3 sloped lines are for indication only.

close, as a function of time (Figure 10A), as well as in steady state as a function of Sc (Figure 10B).

Scalar transfer in turbulent flow

Homogeneous isotropic turbulence (HIT) in a cubic (side length L), fully periodic domain is generated by means of linear forcing.[14] The volume-averaged velocity is zero at any moment in time. In addition to L, input variables are the kinematic viscosity of the liquid ν, and the power input per unit mass ε. Under fully developed, steady conditions, ε is equal to the energy dissipation rate and a Kolmogorov length scale can be defined as $\eta_K = (\nu^3/\varepsilon)^{1/4}$. In a developed turbulent field, a solid spherical particle with radius a and density ρ_p is released. The particle is free to move (translate and rotate) under the influence of hydrodynamic forces. The particle does not feel gravity. Our aim is to quantify scalar transfer from particle to liquid. For this we follow the same procedure as earlier in this article: a scalar concentration $c = 1$ is imposed at the surface of the particle (and periodic conditions at all edges of the cubic domain), the concentration field in the liquid is solved, and the Sherwood number is obtained based on integration of $\dot{m}$ according to Eq. 2. Given the continuously changing hydrodynamic environment of the sphere, the Sherwood number will fluctuate in time. In this article, we are mostly interested in its time-average value $\overline{\mathrm{Sh}}$. Dimensional analysis teaches that $\overline{\mathrm{Sh}} = f\left(a/\eta_K, \mathrm{Sc}, \rho_p/\rho\right)$.

In this article, the density ratio is fixed: $\rho_p/\rho = 4$. The Schmidt numbers we are considering are the same as for the benchmark of the flow past a sphere at finite Re: Sc = 10, 30, 100, 300, and 1000. We accommodate for these five Schmidt numbers by solving five concentration fields in conjunction with each solid–liquid flow simulation. Next to computational effectiveness, this has the advantage of being able to compare scalar fields with different diffusivities in exactly the same flow. The ratio a/η_K has been varied between 5.35 and 10.7, that is, $a/\eta_K > 1$. It implies that the smallest turbulent structures are smaller than the particle so that its direct hydrodynamic environment is inhomogeneous (as opposed to $a/\eta_K \ll 1$ for which the sphere would see a time-varying but homogeneous deformation field). Numerical sensitivities have been checked for $a/\eta_K = 10.7$, that is, the highest value and thus the most demanding in terms of resolution, as this case has the finest flow structures relative to the particle size. In terms of the cubic grid spacing, the Kolmogorov scale then is $\eta_K = 0.74\Delta$ and thus $\Delta < \pi\eta_K$ which is the typical criterion for sufficiently resolved DNS of turbulence.[29,30]

The realization that $\overline{\mathrm{Sh}} = f\left(a/\eta_K, \mathrm{Sc}, \rho_p/\rho\right)$ has the advantage that the right-hand side only contains (known) input variables. Its disadvantage is that it does not relate well with the usual Sherwood correlations that are of the form $\overline{\mathrm{Sh}} = f(\mathrm{Re}, \mathrm{Sc})$, for example, Eq. 3 (with Pe = ReSc) and also the widely used Ranz-Marshall correlation $\mathrm{Sh} = 2 + 0.6\mathrm{Re}^{1/2}\mathrm{Sc}^{1/3}$.[31] Correlations of the latter form are for spheres experiencing an average, unidirectional flow for which a Reynolds number can be determined unambiguously. In the current situation (a sphere in HIT with no average, overall flow), the choice for Re is not obvious. It should be a Reynolds number based on the relative velocity between fluid and particle, that is, a slip velocity. A seemingly arbitrary choice to be made, however, is the size of the environment around the sphere to average the fluid velocity over to determine a slip velocity.

The reference simulation has $a = 8\Delta$, a spherical shell with thickness $\delta = 1.5\Delta$ and a grid with $\Delta r = \delta/64$ and $\Delta\theta = \Delta\varphi = \pi/40$. The cubic domain has side length $L/a = 16$ and the turbulence is such that $a/\eta_K = 10.7$. This spherical grid is much finer than in the benchmarks as we expect more complex flow around the sphere. The domain size relative to the Kolmogorov length scale is $L/\eta_K \approx 170$. In earlier work,[19,32] we have shown that this dynamic range of scales is sufficiently wide to develop representative turbulence with a spectrum with a clear inertial and dissipative range.

Impressions of the reference simulation are given in Figure 11. It shows scalar concentration (note the logarithmic scale) in a cross sections through the entire domain and through the center of the sphere at three moments for

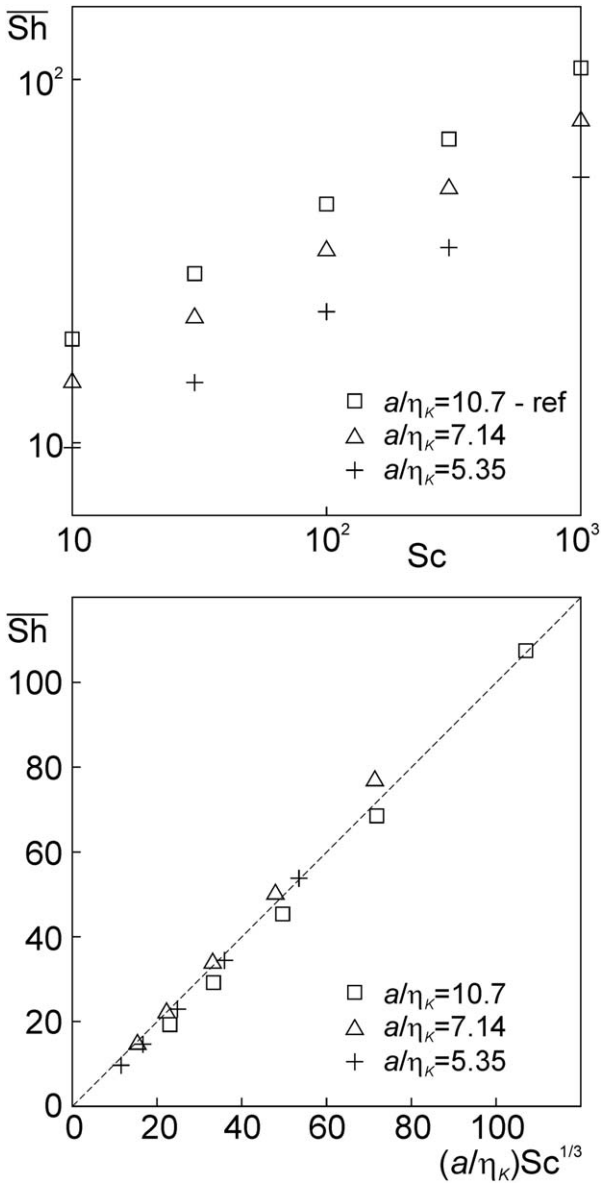

Figure 15. $\overline{Sh}$ vs. Sc, effect of a/η_K.

The lower panel probes the correlation $\overline{Sh} \propto (a/\eta_K)Sc^{1/3}$. Reference case grids.

$Sc = 100$. It also shows a velocity vector field in the same cross section. Clearly, the sphere transfers scalar into the liquid that is subsequently caught by the vortical structures in the turbulent field around the sphere. From the vector plot, it can be assessed that eddies smaller than the sphere exist, in accordance with the notion $a/\eta_K > 1$.

In Figure 12, instantaneous realizations of the concentration in the spherical shell are shown. These inhomogeneous concentration fields indicate that release of scalar varies strongly over the sphere's surface and in fluctuating patterns, very different from the coherent and steady fields shown for one of the benchmarks in Figure 6. Strong radial gradients can be inferred from comparing the fields at the two radial locations (halfway the shell thickness, and at the outer surface of the shell). An increase of the Schmidt number makes the concentration structures narrower. It also can be seen that for $Sc = 1000$ numerical wiggles start appearing indicating that we are close to resolution limits for this high (but practically relevant) value of the Schmidt number.

The time evolution of the overall (i.e., integrated over the surface of the sphere) scalar transfer process is presented in Figure 13 (upper panel) as time series of the Sherwood number (determined via application of Eq. 2) for the reference cases and three of the five Schmidt numbers. After a very short transient—that spans over of the order of 10 Kolmogorov time scales—at initial stages when the sphere encounters fresh ($c = 0$) liquid, the Sherwood numbers become dynamically steady with a pronounced dependency on the Schmidt number. Fluctuation levels are of the order of 30% of the time-average Sherwood values. The mutual coherence of the Sherwood time series for the three different Schmidt numbers is the result of the same flow dynamics felt by the different scalars.

For later analysis and interpretation, Reynolds numbers based on slip velocity are tracked with sample results in the lower panel of Figure 13. As noted before, there is no unambiguous way to determine the liquid velocity term in the slip velocity for the cases here that have no average flow. The two curves in the lower panel of Figure 13 relate to the size of the hydrodynamic environment around the sphere over which the liquid velocity was averaged. The curve with $D = 16a$ comprises the full domain for averaging. The high frequency scatter in the curve with $D = 4a$ is not a numerical instability; instead it is due to the stepwise change of the nodes involved in the averaging as the sphere moves over the cubic grid. There is no direct coherence between the signals in the upper and lower panel of Figure 13 which means that an instantaneous Reynolds number does not directly determine the instantaneous Sherwood number. This also is not to be expected given the small scale details—much smaller than $D = 4a$, let alone $D = 16a$—near the sphere that determine mass transfer. The average Reynolds number of the smaller environment is some 30% lower than of the larger environment.

Further analysis is done in terms of time-averaged quantities and will focus on assessment of grid resolution, the effects of the strength of the turbulence (measure a/η_K) on the scalar transfer process, and on comparison with scalar transfer correlations.[6,31]

The two panels of Figure 14 show to what extent $\overline{Sh}$ depends on the grids. The impact of the grid in radial direction in the spherical shell is marginal as can be seen in the left panel. The left panel also shows the limited effect of the orientation of the spherical grid. If it is rotated over 90° (from x-orientation to z-orientation) while the sphere is exposed to exactly the same flow, average Sherwood numbers change by less than 0.3%. The resolution of the cubic grid (right panel of Figure 14) has a more significant and systematic influence on $\overline{Sh}$. From the coarsest to the finest grid, the average Sherwood number reduces by some 2.5%. The data as plotted on the logarithmic scales of Figure 14 hint at an approximate $Sc^{1/3}$ dependency of $\overline{Sh}$.

In subsequent simulations, the turbulence is weakened compared to the reference case, that is, the energy dissipation rate ε is reduced. This increases the Kolmogorov length scale and thus reduces a/η_K (at constant particle radius a). To sustain turbulence and to have the same ratio of largest over smallest turbulent length scale in the simulations with weaker turbulence, the ratio L/η_K is kept constant to 170. Reducing a/η_K therefore also means larger domains; the case with $a/\eta_K = 10.7$ has $L = 128\Delta$, the case with $a/\eta_K = 5.35$ has $L = 256\Delta$. To keep the simulations affordable, the resolution

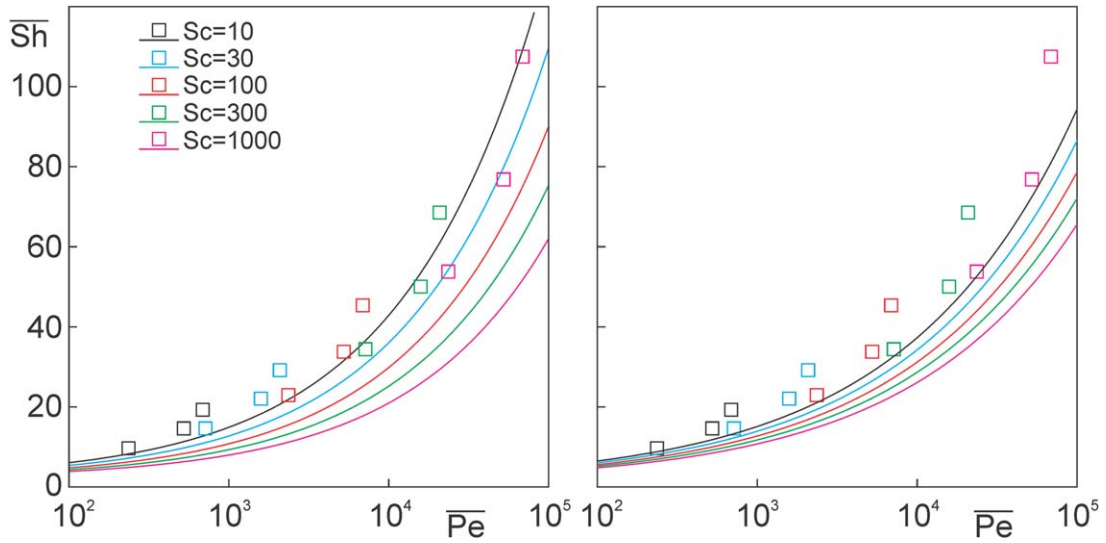

Figure 16. Comparison of simulation results with mass transfer correlations.

$\overline{\mathrm{Sh}}$ vs. $\overline{\mathrm{Pe}}=\overline{\mathrm{Re}}\mathrm{Sc}$. Left: Ranz-Marshall correlation $\overline{\mathrm{Sh}}=2+0.6\overline{\mathrm{Pe}}^{1/2}\mathrm{Sc}^{-1/6}$; Right: Eq. 3. In the correlations the time-averaged Reynolds number is based on the slip velocity with the liquid velocity averaged over a cubic domain with side length $D=16a$. Curves: correlations; symbols: simulations. [Color figure can be viewed in the online issue, which is available at wileyonlinelibrary.com.]

of the cubic grid was kept at its lowest value: $a=8\Delta$ and we realize—given the results in Figure 9D and particularly in Figure 14 (right panel)—that we are overestimating $\overline{\mathrm{Sh}}$; Figure 14 suggests by some 2.5%.

As expected, the scalar transfer rates get smaller in weaker turbulence, see Figure 15. The data suggest a proportionality of $\overline{\mathrm{Sh}}$ with a/η_K. This has been further detailed in Figure 15 (lower panel) where we show that the simulation results can be correlated according to $\overline{\mathrm{Sh}} \approx \alpha \frac{a}{\eta_K}\mathrm{Sc}^{1/3}$, with the proportionality constant α approximately equal to 1.

Finally, we investigate (in Figure 16) to what extent the trends in $\overline{\mathrm{Sh}}$ with flow conditions and Schmidt number are captured by the traditional Sherwood correlations, viz. Eq. 3 and the Ranz-Marshall correlation. Compared to the correlations, the simulation results predict systematically higher $\overline{\mathrm{Sh}}$ values. Ratios of simulation results and correlation results get as large as two, which conversely means that the orders of magnitude are the same. The $\overline{\mathrm{Sh}}$ trends with $\overline{\mathrm{Pe}}=\overline{\mathrm{Re}}\mathrm{Sc}$ (the overbar meaning time averaging) and Sc are the same as well. At constant Sc, however, $\overline{\mathrm{Sh}}$ increases more steeply with $\overline{\mathrm{Pe}}$ in the simulations as compared to the correlations.

Summary and Conclusions

We have proposed a method for simulation of passive scalar transfer from a solid spherical particle into the liquid the particle is immersed in. The method is specifically designed for moving (translating and rotating) particles where in the simulations the particles are allowed to move relative to a fixed grid that resolves the liquid flow. The specific challenge to overcome for solid–liquid systems is the usually high Schmidt number of the liquid and the (therefore) steep scalar gradients near the solid–liquid interface. Reverting to a very fine grid in the entire flow domain such that these gradients are properly resolved is hardly an option given the computational cost such a simulation would require. Instead, the proposed method uses COD with a spherical grid attached to the solid–liquid interface, and a cubic outer grid. The spherical grid is made sufficiently fine in radial direction to resolve the thin scalar film near the solid surface. The liquid flow is solved on the cubic, outer grid by means of the LB method. Velocity information is communicated from the outer to the inner grid via interpolation. The outer grid also interacts with the inner grid by means of scalar concentration interpolation.

Benchmarks to test the procedure comprised of uniform creeping flow past a sphere and flow past a sphere at finite Reynolds numbers. These benchmarks show that trends of the Sherwood number with Reynolds and Schmidt numbers are captured correctly. Simulation results are more sensitive to the resolution of the outer, cubic grid as they are to the inner, spherical grid. The method has correct convergence behavior, that is, higher levels of accuracy on finer grids. The benchmark results do show some imperfections if we look into the details of the interactions between the two grids with cubic symmetries showing in the—in principle axisymmetric—velocity and concentration fields on the spherical grid. Overall, the grids interact in a consistent manner as was demonstrated by estimating Sherwood numbers independently from the inner and outer concentration solution.

The performance of the method does not deteriorate if the sphere moves relative to the cubic grid. Almost identical solutions were obtained for a fixed sphere and a sphere moving steadily over the grid.

When the sphere is released in a turbulent field such that its size is larger than the Kolmogorov length scale ($a/\eta_K > 1$), the concentration field shows strong temporal and spatial fluctuations; the latter on length scales much smaller than the size of the sphere; the former on time scales of the order 10 Kolmogorov time scales. Time-average Sherwood numbers approximately scale with $\mathrm{Sc}^{1/3}$ and a/η_K.

A main objective of future work is to extend the method to (moderately) dense solid–liquid suspensions, that is, systems having more than one solid sphere. A major hurdle to overcome is dealing with overlapping spherical shells of particles in each other's vicinity. Directly solving convection

diffusion equations for such multiple-sphere geometries on grids adapted to sphere doublets (or triplets,...) does not seem a computationally feasible option with hundreds of spheres in one simulation. Instead, we think along lines of devising mixing rules in overlapping cells of two different shells. The fact that the method allows for thin shells indicates that only small amounts of scalar would be involved in such possibly speculative mixing rules. Other avenues for future research will focus on improving the method's accuracy and further suppressing imperfections by investigating other interpolation schemes.

Literature Cited

1. Lawrence AE, Sherwood TK. Heat transmission to water flowing in pipes. *Ind Eng Chem.* 1931;23:301–309.
2. Kramers H. Heat transfer from spheres to flowing media. *Physica* 1946;12:61–80.
3. Piret EL, James W, Stacey M. Heat transmission from fine wires to water—low velocity data and correlation. *Ind Eng Chem.* 1947;9: 1098–1103.
4. Whitaker S. Forced convection heat transfer correlations for flow in pipes, past flat plates, single cylinders, single spheres and for flow in packed beds and tube bundles. *AIChE J.* 1972;18:361–371.
5. Bird RB, Stewart WE, Lightfoot EN. *Transport Phenomena*. New York: Wiley, 1960.
6. Clift R, Grace JR, Weber ME. *Bubbles, Drops, and Particles*. New York: Academic Press, 1978.
7. Feng ZG, Michaelides EE. Heat transfer in particulate flows with direct numerical simulation (DNS). *Int J Heat Mass Transfer*. 2009; 52:777–786.
8. Ambesi D, Kleijn CR. Laminar-forced convection mass transfer to ordered and disordered single layer arrays of spheres. *AIChE J*. 2013;59:1400–1408.
9. Deen NG, Kriebitzsch SHL, Van der Hoef MA, Kuipers JAM. Direct numerical simulation of flow and heat transfer in dense fluid-particle systems. *Chem Eng Sci*. 2012;81:329–344.
10. Ponoth SS, McLaughlin JB. Numerical simulation of mass transfer for bubbles in water. *Chem Eng Sci*. 2000;55:1237–1255.
11. Radl S, Tryggvason G, Khinast JG. Flow and mass transfer of fully resolved bubbles in non-Newtonian fluids. *AIChE J*. 2007;53:1861–1878.
12. Tryggvason G, Dabiri S, Aboulhasanzadeh B. Multiscale considerations in direct numerical simulations of multiphase flows. *Phys Fluids*. 2013;25:031302.
13. Bothe D, Fleckenstein, S. A volume-of-fluid-based method for mass transfer processes at fluid particles. *Chem Eng Sci*. 2013;101:283–302.
14. Rosales C, Meneveau C. Linear forcing in numerical simulations of isotropic turbulence: physical space implementations and convergence properties. *Phys Fluids*. 2005;17:095106-1–095106-8.
15. Chen S, Doolen GD. Lattice Boltzmann method for fluid flows. *Annu Rev Fluid Mech.* 1989;30:329–364.
16. Succi S. *The Lattice Boltzmann Equation for Fluid Dynamics and Beyond*. Oxford: Clarendon Press, 2001.
17. Goldstein D, Handler R, Sirovich L. Modeling a no-slip flow boundary with an external force field. *J Comput Phys*. 1993;105:354–366.
18. Derksen JJ, Sundaresan S. Direct numerical simulations of dense suspensions: wave instabilities in liquid-fluidized beds. *J Fluid Mech*. 2007;587:303–336.
19. Derksen JJ. Direct numerical simulations of aggregation of monosized spherical particles in homogeneous isotropic turbulence. *AIChE J*. 2011;58:2589–2600.
20. Ronchi C, Iacono R, Paolucci PS. The "cubed sphere": a new method for the solution of partial differential equations in spherical geometry. *J Comput Phys*. 1996;124:93–114.
21. Harten A. High resolution schemes for hyperbolic conservation laws. *J Comput Phys*. 1983:49;357–364.
22. Sweby PK. High resolution schemes using flux limiters for hyperbolic conservation laws. *SIAM J Numer Anal*. 1984;21:995–1011.
23. Wang Y, Hutter K. Comparison of numerical methods with respect to convectively dominated problems. *Int J Numer Methods Fluids*. 2001;37:721–745.
24. Hartmann H, Derksen JJ, Van den Akker HEA. Mixing times in a turbulent stirred tank by means of LES. *AIChE J*. 2006;52:3696–3706.
25. Caiazzo A. Analysis of lattice Boltzmann nodes initialisation in moving boundary problems. *Prog Comput Fluid Dyn*. 2008;8:3–10.
26. Yang C, Zhang J, Koch DL, Yin X. Mass/heat transfer from a neutrally buoyant sphere in simple shear flow at finite Reynolds and Peclet numbers. *AIChE J*. 2011;57:1419–1433.
27. Feng Z, Michaelides EE. Mass and heat transfer from fluid spheres at low Reynolds numbers. *Powder Technol*. 2000;112:63–69.
28. Feng Z-G, Michaelides EE. A numerical study on the transient heat transfer from a sphere at high Reynolds and Peclet numbers. *Int J Heat Mass Transfer*. 2000;43:219–229.
29. Moin P, Mahesh K. Direct numerical simulation: a tool in turbulence research. *Annu Rev Fluid Mech*. 1998;30, 539–578.
30. Eswaran V, Pope SB. An examination of forcing in direct numerical simulations of turbulence. *Comput Fluids*. 1988;16:257–278.
31. Ranz WE, Marshall WR. Evaporation from drops. *Chem Eng Prog*. 1952;48:142–180.
32. Derksen JJ. Flow induced forces in sphere doublets. *J Fluid Mech*. 2008;608:337–356.

Manuscript received Aug. 25, 2013, and revision received Nov. 27, 2013.